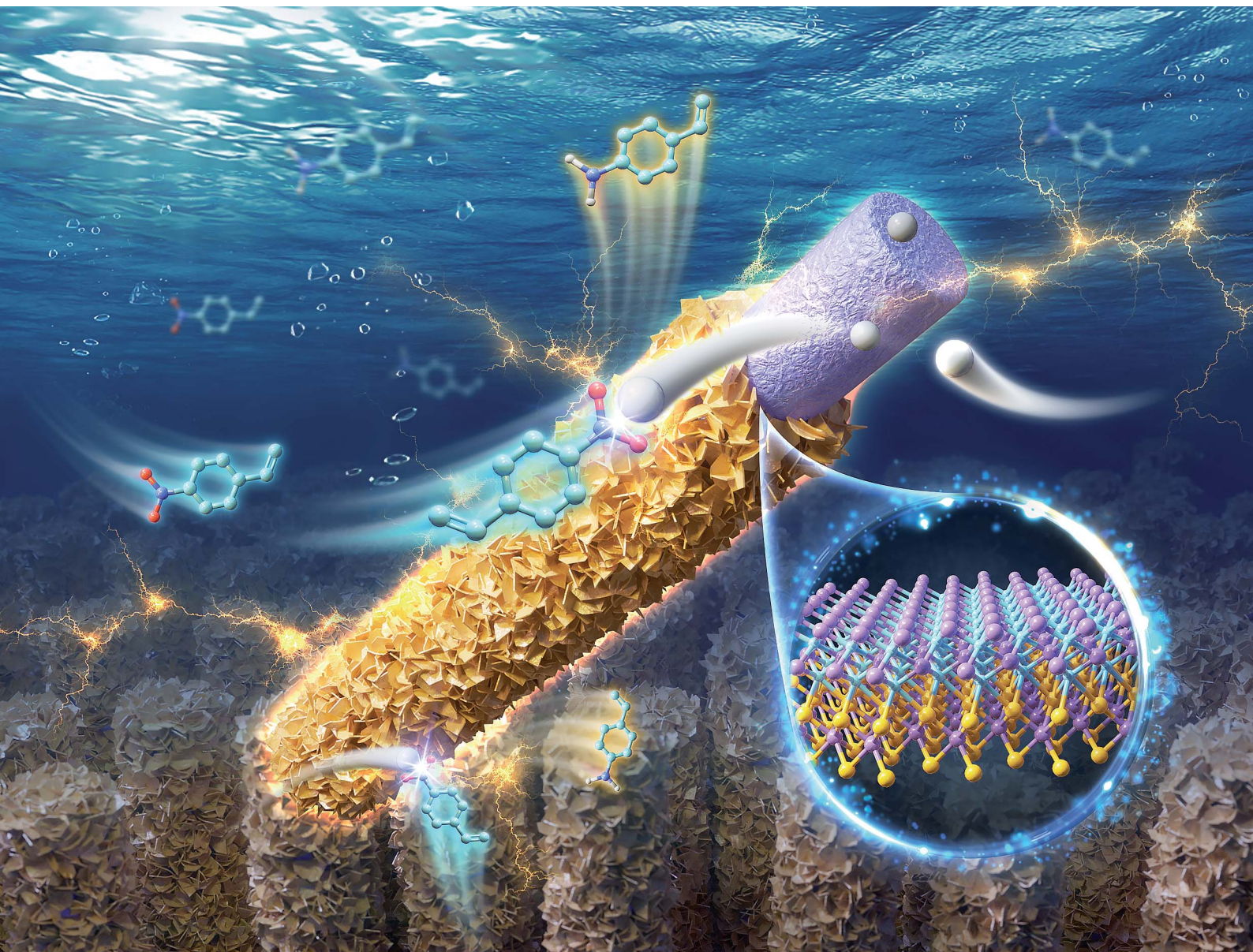


Chemical Science

Volume 15
Number 10
14 March 2024
Pages 3395–3770

rsc.li/chemical-science



ISSN 2041-6539

EDGE ARTICLE

Wenbiao Zhang, Qingsheng Gao *et al.*
Synergistic enhancement of electrocatalytic nitroarene
hydrogenation over $\text{Mo}_2\text{C}@\text{MoS}_2$ heteronanorods with
dual active-sites

Cite this: *Chem. Sci.*, 2024, 15, 3446

All publication charges for this article have been paid for by the Royal Society of Chemistry

Synergistic enhancement of electrocatalytic nitroarene hydrogenation over Mo₂C@MoS₂ heteronanorods with dual active-sites†

Wanling Zhang,^a Wenbiao Zhang,^{*ab} Kun Yu,^a Jingwen Tan,^a Yi Tang^{id b} and Qingsheng Gao^{id *a}

Electrocatalytic hydrogenation (ECH) enables the sustainable production of chemicals under ambient conditions, in which catalysts catering for the different chemisorption of reactants/intermediates are desired but still challenging. Here, Mo₂C@MoS₂ heteronanorods with dual active-sites are developed to accomplish efficient nitroarene ECH according to our theoretical prediction that the binding of atomic H and nitro substrates would be synergistically strengthened on Mo₂C–MoS₂ interfaces. They afford high faradaic efficiency (>85%), yield (>78%) and selectivity (>99%) for the reduction of 4-nitrostyrene (4-NS) to 4-vinylaniline (4-VA) in neutral electrolytes, outperforming not only the single-component counterparts of Mo₂C nanorods and MoS₂ nanosheets, but also recently reported noble-metals. Accordingly, *in situ* Raman spectroscopy combined with electrochemical tests clarifies the rapid ECH of 4-NS on Mo₂C–MoS₂ interfaces due to the facilitated elementary steps, quickly refreshing active sites for continuous electrocatalysis. Mo₂C@MoS₂ further confirms efficient and selective ECH toward functional anilines with other well-retained reducible groups in wide substrate scope, underscoring the promise of dual-site engineering for exploring catalysts.

Received 9th November 2023
Accepted 5th February 2024

DOI: 10.1039/d3sc06010a

rsc.li/chemical-science

Introduction

Renewable electricity powered chemical processes are burgeoning for the sustainable production of high-value chemicals.^{1–3} In particular, electrocatalytic hydrogenation (ECH) utilizes electrochemically formed hydrogen H* (* denotes an active site) from protons/water to upgrade various groups (*e.g.*, carbonyl, nitro, alkenyl, *etc.*) under ambient conditions,^{4–9} avoiding harsh operations associated with high temperature and H₂ pressure adopted in thermocatalysis. For example, the reduction of nitroarenes to anilines is significant for manufacturing medicine, dyes, spices, and explosives.¹⁰ Witnessed progress has been made in the thermocatalytic hydrogenation of nitroarenes using H₂,^{11–13} but it is challenged by the trade-off between activity and selectivity due to the difficult control over reaction pathways under heated and

pressurized conditions.^{10,14} ECH, at room temperature and atmospheric pressure, neatly offers a controllable alternative to accommodate such multi-electron transfer processes *via* varying working potentials or currents.^{6,15} Following a typical Langmuir–Hinshelwood (L–H) mechanism,^{16,17} ECH proceeds *via* the stepwise reactions of adsorbed organics and H* on the catalyst surface, highly dependent on their competitive chemisorption. As H* is dominant, the hydrogen evolution reaction (HER) *via* its self-combination occurs easily, decreasing the faradaic efficiency (FE) of ECH,¹⁸ while the bimolecular coupling of nitroarenes or aldehydes/ketones toward azoxybenzenes or pinanols would exceed the target hydrogenation when the coverage of adsorbed organics is excessively high.^{19,20} It is necessary to design a catalyst surface that can counterbalance the difference in chemisorption toward efficient hydrogenation.^{21,22}

As a noble-metal-free electrocatalyst, MoS₂ demonstrates its efficiency in the ECH of aldehydes and nitroarenes;^{16,23} however, the sluggish H₂O activation and discharging to H* (H₂O + e[−] → H* + OH[−]) under basic/neutral conditions unfortunately limit ECH kinetics. Efforts have been devoted to creating lattice defects and adjusting the phase transition,^{23,24} which fail to balance the competitive chemisorption of H* and organic substrates due to non-selective enhancement on a single kind of active sites. Constructing heterointerfaces involving dual active sites would be a promising alternative. The combination of MoS₂ with noble-metals is capable of accommodating the

^aCollege of Chemistry and Materials Science, Guangdong Provincial Key Laboratory of Functional Supramolecular Coordination Materials and Applications, Jinan University, Guangzhou 510632, P. R. China. E-mail: wbzhang1994@hotmail.com; tqsgao@jnu.edu.cn

^bDepartment of Chemistry, Shanghai Key Laboratory of Molecular Catalysis and Innovative Materials, Laboratory of Advanced Materials and Collaborative Innovation Centre of Chemistry for Energy Materials, Fudan University, Shanghai 200433, P. R. China

† Electronic supplementary information (ESI) available: Additional figures and data for degrader evaluation, EDS mapping, additional XRD, XPS and CVs, and details of NMR spectra. See DOI: <https://doi.org/10.1039/d3sc06010a>



different elementary steps of multi-electron transfer processes (e.g., N_2 and H_2O reduction),^{25–27} but cannot meet the requirement of ECH because of the seriously retarded FEs and increased operation cost after introducing precious elements highly active for the HER.²⁸

Thanks to the relatively more favorable H_2O activation and stronger binding with H^* ,^{29–31} noble-metal-like molybdenum carbides (Mo_xC) would be available to construct qualified interfaces on MoS_2 . Moreover, such two moieties share the same Mo element, enabling the facile construction and proliferative synergy of their interfaces. Here, $Mo_2C@MoS_2$ with dual sites was developed to enable the efficient ECH of nitroarenes. As indicated by density functional theory (DFT) calculations, the binding of H^* and 4-nitrostyrene (4-NS^{*}) was strengthened on the Mo_2C and nearby MoS_2 of Mo_2C-MoS_2 interfaces, respectively, which would promote the surface elementary steps of hydrogenation. As expected, $Mo_2C@MoS_2$ heteronanorods consisting of Mo_2C axes and MoS_2 shells accomplished high FE (>85%), selectivity (>99%) and yield (>78%) for the ECH of 4-NS to 4-vinylaniline (4-VA) in neutral electrolytes at -0.05 to -0.45 V vs. RHE, superior to single-component Mo_2C nanorods and MoS_2 nanosheets and even recently reported noble-metals. *In situ* Raman spectroscopy further confirmed the rapid ECH of 4-NS on Mo_2C-MoS_2 interfaces, quickly refreshing active sites for continuous electrocatalysis. In sharp comparison, the slow turnover due to the absence of either effective nitro activation on Mo_2C or rich H^* on MoS_2 spawned the accumulation of hydrophobic reactants/intermediates and consequently an extra interfacial impedance on electrodes verified by electrochemical impedance spectroscopy (EIS). Moreover, $Mo_2C@MoS_2$ afforded efficient and selective ECH toward functional anilines in wide substrate scope, highlighting its efficiency for electrocatalytic refinery.

Experimental section

Chemicals

Ammonium molybdate tetrahydrate ($(NH_4)_6Mo_7O_{24} \cdot 4H_2O$, AHM), aniline, thiourea and hydrochloric acid (HCl, AR) were purchased from Sinopharm Chemical Reagent Co. Ltd (Shanghai, China). 4-Nitrostyrene and Nafion solution (5 wt% in lower aliphatic alcohols and water) were purchased from Sigma-Aldrich. All chemicals were of analytical grade and used as received without further purification. All aqueous solutions were prepared using ultrapure water (>18.2 M Ω).

Material synthesis

Synthesis of Mo_2C nanorods. The synthesis of Mo_2C nanorods was conducted according to our previous report.³² Specifically, 2.48 g AHM and 3.23 mL aniline were dissolved in 40 mL ultrapure water and adjusted to pH 4.0–4.5 by adding 1.0 mol L⁻¹ HCl. The above solution was sealed and transferred to an oil bath at 50 °C for 5 hours while being stirred. Then, the as-received $Mo_3O_{10}C_6H_8N_2 \cdot 2H_2O$ nanowires were gathered and rinsed several times with ethanol and deionized water, respectively, and dried in a vacuum oven. To fabricate Mo_2C nanorods,

the above precursors (0.15 g) were annealed under an Ar flow at 775 °C for 5 hours.

Synthesis of MoS_2 nanosheets. AHM (0.35 g) and thiourea (1.83 g) were dissolved in 10 mL of ultrapure water in a 20-mL Teflon-lined stainless-steel autoclave and heated at 240 °C for 3 hours. Afterwards, the solid was washed and collected by centrifugation with both water and ethanol several times. MoS_2 nanosheets were finally obtained by overnight drying at 50 °C under vacuum.

Synthesis of $Mo_2C@MoS_2$ nanorods. $Mo_2C@MoS_2$ nanorods were synthesized *via* a controllable surface oxidation of Mo_2C nanorods followed by a hydrothermal sulfidation approach. In detail, the above prepared Mo_2C nanorods (0.3 g) were placed in a crucible and oxidized at 200 °C under an air flow for 30 min. And then, the obtained samples (0.1 g) and thiourea (1.0 g) were dispersed and ultrasonicated in 10 mL of water to obtain the homogeneous solution. Subsequently, this solution was transferred into a 20 mL Teflon-lined stainless-steel autoclave and heated at 240 °C for 3 hours. Finally, the black solid was washed and collected by centrifugation with water and ethanol several times. $Mo_2C@MoS_2$ nanorods were finally received after drying at 50 °C in a vacuum overnight.

Physical characterization

X-ray diffraction (XRD) analysis was conducted on a Bruker D8 Advance diffractometer with Cu K α radiation ($\lambda = 1.54056$ Å). Transmission electron microscopy (TEM) and scanning electron microscopy (SEM) were conducted on a JEOL JEM-2100F and ZEISS ULTRA 55, respectively. X-ray photoelectron spectroscopy (XPS) was carried out on a Thermo Fisher Scientific (Escalab 250Xi), and the binding energy was calibrated with respect to the C 1s (284.6 eV) of contaminated carbon. Raman spectra were collected on a LabRAM HR Evolution, with an excitation laser wavelength of 532 nm. Nitrogen adsorption-desorption isotherms were used to determine the specific surface areas of electrocatalysts on an automatic gas adsorption analyzer (Quantachrome Autosorb-iQ-MP) by a multipoint Brunauer-Emmett-Teller (BET) method. Electron paramagnetic resonance (EPR) spectra were recorded on a Magnetech ESR500.

Electrochemical test

To prepare working electrodes, 10 mg of electrocatalysts and 100 μ L of 5 wt% Nafion solution were dispersed in 1.0 mL water-ethanol with a $V_{water}/V_{ethanol}$ ratio of 4:1 and then the mixture was vigorously sonicated for at least 30 min to get a homogeneous ink. The as-obtained ink (500 μ L) was loaded onto pre-treated carbon cloth (1.5 cm \times 1.5 cm) carefully and dried naturally in air. The working electrode was directly subjected to the ECH of nitroarenes, which was conducted on a CHI 650E electrochemical workstation (Chenhua Instruments Shanghai Co., Ltd, China), within a gas-tight two-compartment electrochemical cell equipped with a piece of a proton-exchange membrane (Nafion 117) as the separator. A saturated calomel electrode (SCE) and a platinum electrode were used as the reference and counter electrodes, respectively. The cathodic



electrolyte (pH 6.8) contained 4-NS (12.5 mmol L⁻¹), LiClO₄ (0.1 mol L⁻¹) and methanol/water (1 : 1), which was degassed using a N₂ gas flow for 30 min prior to the ECH and saturated with the same flow-rate N₂ during the test. Methanol was used to improve the homogeneous dispersion of the 4-NS phase in the electrolyte. Linear sweep voltammetry (LSV) was conducted in an undivided cell with and without 12.5 mmol L⁻¹ 4-NS in 40 mL LiClO₄ solutions (pH 6.8).

To identify the involvement of H* during the ECH, EPR measurement with 5,5-dimethyl-1-pyrroline-N-oxide (DMPO) as the trapping agent was conducted. After the chronoamperometry test at a given constant potential of -0.45 V vs. RHE for 5 min, 0.1 mM DMPO was added into the cathodic electrolyte and stirred for 1 min. Afterwards, the electrolyte was taken out for the EPR test. Meanwhile, *t*-BuOH (25 wt% in 0.1 M LiClO₄) was used to quench hydrogen radicals during chronoamperometry at -0.45 V vs. RHE, in which 4-VA was detected every 60 min. The obviously prohibited yield of 4-VA in comparison with that free-from *t*-BuOH again proved the involvement of H*.

Product analysis

After reactions, liquid products were collected from the cathode compartment and analyzed *via* a HPLC (SHIMADZU LC-20AT) equipped with a UV detector at 254 and 370 nm. The column (INERTSUSTAIN C18) was operated at 40 °C and the binary gradient method was adopted at a flow rate of 0.8 mL min⁻¹, which contained H₂O and CH₃OH (*V*_{CH₃OH} : *V*_{H₂O} = 6 : 4). The FE (%), yield (%) and selectivity (%) of products were calculated based on the following equations:

$$\text{FE (\%)} = \frac{\text{mole of hydrogenation product} \times z \times F}{\text{total charge used}} \times 100\%$$

$$\text{Yield (\%)} = \frac{\text{mole of hydrogenation product}}{\text{mole of theoretical aromatic amine}} \times 100\%$$

$$\text{Selectivity (\%)} = \frac{\text{mole of target hydrogenation product}}{\text{mole of total products}} \times 100\%$$

where, *z* is the number of transferred electrons, which for 4-VA, 4-ethyl-nitrobenzene (4-ENB) and 4-ethylaniline (4-EA) is 6, 2 and 8, respectively. *F* is the faradaic constant (96 485 C mol⁻¹).

Theoretical calculations

In this work, all the theoretical computations were based on the DFT method, as implemented in the CASTEP package of Materials Studio. For the exchange–correlation functional, we used the generalized gradient approximation (GGA) with the Perdew–Burke–Ernzerhof (PBE) functional. The projector augmented wave (PAW) method was applied to depict the interaction between ion and electron, and the cut of energy was set at 400.0 eV. The force and energy cutoff were set at 0.01 eV Å⁻¹ and 10⁻⁶ eV for the geometry optimization, respectively. A 5

× 5 × 1 Monkhorst–Pack grid *k*-point sampling was conducted for the bulk and slab structure optimization. The optimized bulk Mo₂C (space group: *P*6₃/*mmc*; *a* = *b* = 3.0 Å, *c* = 4.7 Å) and 2H–MoS₂ (space group: *P*6₃/*mmc*; *a* = *b* = 3.2 Å, *c* = 12.3 Å) were selected. Then, we selected a 3 × 3 relaxed rhombus MoS₂(002) bilayer on top of the relaxed 4 × 4 Mo₂C(001) surface to model Mo₂C–MoS₂ heterojunctions, in which S atoms were introduced to saturate the coordination of Mo atoms on the Mo₂C(001). The adsorption slab would be curved as the (010) of the Mo₂C–MoS₂ layer and a vacuum layer of 12 Å was used to isolate the slab as the boundary condition, which made the interactions between neighboring slabs negligible according to other previous work.³³

The binding energy (BE) of an adsorbate was calculated as:

$$\text{BE}_{(\text{adsorbate})} = E_{(\text{slab+adsorbate})} - E_{(\text{slab})} - E_{(\text{adsorbate})\text{W}}$$

here *E*_(slab+adsorbate), *E*_(slab) and *E*_(adsorbate) are the energies of a slab with the adsorbate and the pure slab/facet and the adsorbate in the gas phase, respectively. The *E*(H) is taken as one half the total energy of the H₂ molecule during the calculation of H binding energy.

Results and discussion

DFT calculations were conducted to analyze the varied binding energies of H* (BE_H) and 4-NS* (BE_{4-NS}) on MoS₂, Mo₂C and their interfaces. According to previous reports^{34,35} and the experimentally evidenced selective hydrogenation of the nitro group in this work, the vertical chemisorption of 4-NS *via* bonding nitro with Mo sites was reasonably taken into account.³⁶ In further regard to H*, the Mo atom on the Mo₂C(101) surface was indicated as the available site because of the obviously stronger BE_H (-0.68 eV) than that on a carbon site (+0.19 eV) (Fig. S1, ESI†), which also exceeded those on the Mo (-0.14 eV) and S sites (-0.1 eV) of MoS₂. For a reliable comparison, the Mo sites on Mo₂C, MoS₂ and Mo₂C–MoS₂ models were further considered in the context of the competitive chemisorption of 4-NS* and H*. As depicted in Fig. 1a, the edge-site rich MoS₂(010) presented obviously weaker binding with H* (-0.14 eV) but the stronger one with 4-NS* (-1.39 eV) relative to Mo₂C (101) (BE_H: -0.68 eV; BE_{4-NS}: -0.48 eV), which suggested the favorable activation of nitro on MoS₂ and the rich H* on Mo₂C when these sites were combined together. As expected, a Mo₂C–MoS₂ interface showed the synchronously strengthened BE_H (-0.73 eV) on Mo₂C and BE_{4-NS} (-2.77 eV) on MoS₂ (Fig. 1b), in favor of the ECH *via* the L-H mechanism. Accordingly, the projected density of states (PDOS) for d bands (Fig. 1c) was visibly broadened near the Fermi level (*E*_F) on Mo₂C–MoS₂, benefiting the chemisorption of either H* or 4-NS* due to the easy overlap of orbitals. In the chemisorption configurations (Fig. 1d), the electron density distribution of 4-NS* on MoS₂ was closer than that on Mo₂C, confirming its more favorable activation on the MoS₂ moiety. It's thus reasonable to design Mo₂C–MoS₂ interfaces to boost 4-NS reduction thanks to the capability of counterbalancing the difference between H* and 4-NS* (Fig. 1e). The ECH of 4-NS can produce 4-VA and 4-



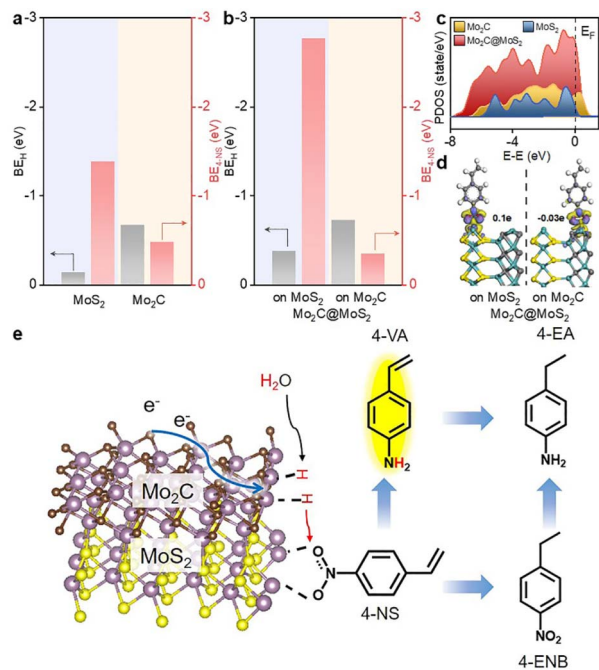


Fig. 1 BE_H and BE_{4-NS} on (a) Mo₂C and MoS₂, and (b) Mo₂C–MoS₂ interfaces. (c) PDOS of Mo₂C, Mo₂C–MoS₂ and MoS₂. (d) Electron density difference of Mo₂C@MoS₂ with 4-NS adsorbed on the Mo₂C or MoS₂ moiety. (e) Schematic illustration for the boosted ECH of 4-NS on Mo₂C–MoS₂ interfaces.

ENB *via* selectively hydrogenating nitro and vinyl groups, respectively, both of which would be further reduced to 4-EA. 4-VA is targeted due to its high added-value for chemical synthesis.

Here, the sequent carbonization and sulfidation of Mo₃-O₁₀(C₆H₈N)₂·2H₂O nanowires (Fig. S2, ESI[†]) was employed to fabricate Mo₂C@MoS₂ heteronanorods for efficient hydrogenation (Fig. 2a). XRD analysis confirmed the co-presence of Mo₂C and MoS₂ phases in Mo₂C@MoS₂ (Fig. 2b), in which the (100), (002) and (101) of Mo₂C and the (002), (101) and (110) of MoS₂ were observed. Accordingly, it showed the characteristic E_{2g}, A_{1g} and 2LA(M) vibration modes of MoS₂, while Mo₂C was transparent in Raman spectra (Fig. S3, ESI[†]). As shown in SEM and TEM (Fig. 2c), Mo₂C@MoS₂ retained the rod-like morphology of parent Mo₂C, but generated nanosheet shells on the surface, resulting in a hierarchical structure that combines the structural merits of 1D Mo₂C (Fig. S4, ESI[†]) and 2D MoS₂ (Fig. S5, ESI[†]). High-resolution TEM (HR-TEM) clearly identified the Mo₂C–MoS₂ interfaces with visible Mo₂C(101) and MoS₂(002) lattices (Fig. 2d). Besides, the corresponding elemental mapping confirmed the uniform distribution of Mo, S, and C in Mo₂C@MoS₂ (Fig. S6, ESI[†]). Such a hierarchical 1D@2D nanostructure enabled its relatively larger surface area of 39.5 m² g⁻¹ (Fig. S7, ESI[†]), as compared to Mo₂C (24.9 m² g⁻¹) and MoS₂ (25.0 m² g⁻¹). Moreover, a series of Mo₂C@MoS₂ prepared with different feeding ratios had a similar nanostructure (Fig. S8 and S9, ESI[†]). In addition, the chemical states of elements were analyzed by XPS (Fig. 2e, f and Table S1, ESI[†]).

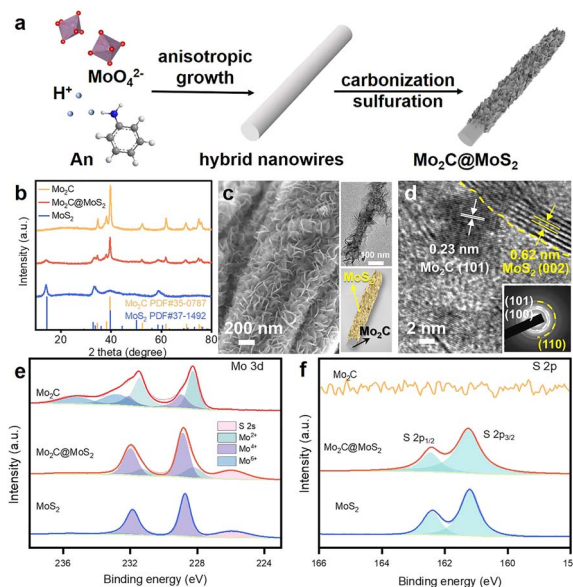


Fig. 2 (a) Schematic illustration for the preparation of hierarchical Mo₂C@MoS₂ nanorods. (b) XRD patterns, (c) SEM and (d) TEM images of Mo₂C@MoS₂ heteronanorods. (e) Mo 3d, (f) S 2p XPS spectra of Mo₂C, Mo₂C@MoS₂ and MoS₂.

In the deconvoluted Mo 3d profile, the doublets at 228.3 and 231.4 eV were ascribed to the Mo 3d_{5/2} and Mo 3d_{3/2} of Mo²⁺ due to the presence of Mo₂C, and those at 228.7 and 231.8 eV corresponded to Mo⁴⁺ of MoS₂.³⁷ The S 2p profile also indicated the consistent chemical state of S in Mo₂C@MoS₂ and MoS₂.

The ECH performances of Mo₂C, MoS₂ and Mo₂C@MoS₂ were tested in a H-type cell separated by a proton exchange membrane (Nafion 117). Cyclic voltammetry (CV) curves were collected in 0.1 M LiClO₄ solution (pH = 6.8) containing 50 wt% methanol to improve the solubility of 4-NS (Fig. S10, ESI[†]), which exhibited a cathodic reduction peak at -0.29 to -0.50 V *vs.* RHE, corresponding to the stepwise reduction.³⁸ Then, their polarization curves in 0.1 M LiClO₄ with and without 4-NS were compared. The cathodic currents of all three catalysts increased after introducing 4-NS and that of Mo₂C@MoS₂ was the highest (Fig. 3a), indicative of its outstanding activity for the ECH. Subsequently, chronoamperometry was performed at -0.05 to -0.45 V *vs.* RHE for 5 h (Fig. 3b). Mo₂C@MoS₂ maintained an obviously higher FE and yield of 4-VA, as compared to Mo₂C and MoS₂. The total FEs were lower than 100% associated with the concomitant HER. At -0.45 V *vs.* RHE, the FE, yield and selectivity of 4-VA were as high as ~85%, ~80%, and 99%, respectively (Fig. 3b and S11, ESI[†]). Furthermore, the electrochemical surface areas (ECSAs) of these electrodes were visualized through calculating the double-layer capacitances (C_{dl}) according to the proportional relationship (Fig. S12, ESI[†]) and subsequently used for normalizing the rate of 4-VA production to access the difference in specific activity. The higher specific reaction rate on Mo₂C@MoS₂ than those on Mo₂C and MoS₂ indicated the intrinsic superiority associated with Mo₂C–MoS₂ interfaces (Fig. S13, ESI[†]). In further comparison with recently reported electrocatalysts including noble-metals (Fig. 3c and



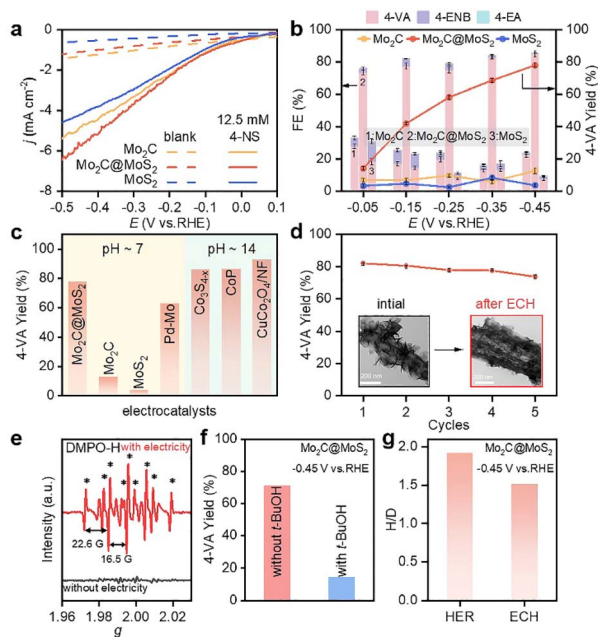


Fig. 3 (a) Polarization curves of Mo_2C , $\text{Mo}_2\text{C}@/\text{MoS}_2$ and MoS_2 in 0.1 M LiClO_4 with and without 12.5 mM 4-NS, and (b) product FEs and yields at -0.05 to -0.45 V vs. RHE with 12.5 mM 4-NS (reaction time: 5 h). (c) Comparison of 4-VA yield of $\text{Mo}_2\text{C}@/\text{MoS}_2$ with that of state-of-the-art electrocatalysts, including Pd–Mo,³⁹ $\text{Co}_3\text{S}_4\text{-x}$,³⁵ CoP,⁴⁰ and $\text{CuCo}_2\text{O}_4/\text{NF}$.⁴¹ (d) Cycle-dependent 4-VA yield over $\text{Mo}_2\text{C}@/\text{MoS}_2$ at -0.45 V. The insets of panel d show the TEM images of $\text{Mo}_2\text{C}@/\text{MoS}_2$ before and after the test. (e) Quasi *in situ* EPR trapping of hydrogen radicals over $\text{Mo}_2\text{C}@/\text{MoS}_2$. (f) Yield of 4-VA with and without *t*-BuOH as the hydrogen radical scavenger. (g) Kinetic isotopic effect of $\text{Mo}_2\text{C}@/\text{MoS}_2$ for the HER and ECH.

Table S2, ESI[†]), $\text{Mo}_2\text{C}@/\text{MoS}_2$ performed among the best and featured mild operation with neutral electrolytes, avoiding the use of alkalis that easily trigger by-reactions (*e.g.*, bi-molecular coupling to azoxybenzenes) and equipment corrosion.

The time-dependent conversion of 4-NS to 4-VA on $\text{Mo}_2\text{C}@/\text{MoS}_2$ was in accordance with the visible decrease of 4-NS and the quick emergence of 4-VA in the HPLC chromatogram (Fig. S14–S16, ESI[†]). The by-product of 4-ENB, derived from the hydrogenation of the vinyl group, was limited to a low level, confirming the highly selective hydrogenation of the nitro group due to the vertical chemisorption. Moreover, $\text{Mo}_2\text{C}@/\text{MoS}_2$ showed stability in repeated ECH tests (Fig. 3d). The slight decrease of 4-VA yield in each cycle should be ascribed to the inevitable loss of the catalyst in the processes of cleaning. The post-test characterization studies (*e.g.*, TEM, XRD and XPS) identified the negligible change of both hierarchical nanostructures and surface states (insets of Fig. 3d, S17 and S18, ESI[†]). In addition, the series of $\text{Mo}_2\text{C}@/\text{MoS}_2$ obtained with the varied feeding ratio showed enhanced activity with the increased amount of thiourea (Fig. S19, ESI[†]), probably thanks to the enriched interfaces.

In order to detect the active species of ECH, quasi *in situ* electron paramagnetic resonance (EPR) spectroscopy coupled with electrochemical tests was conducted with 5,5-dimethyl-1-

pyrroline-N-oxide (DMPO) as the trapping agent (Fig. 3e). The characteristic EPR signals of DMPO-H adducts (nine peaks, $\alpha_{\text{N}} = 16.5$ G and $\alpha_{\text{H}} = 22.6$ G) were visible at -0.45 V vs. RHE, suggesting that the active H^* species was electrochemically generated *via* water reduction.³⁹ Accordingly, when *tert*-butanol (*t*-BuOH) was introduced as a hydrogen radical scavenger, the conversion of 4-NS decreased significantly (Fig. 3f and S20, ESI[†]), confirming H^* as the key intermediate.⁴² Furthermore, the kinetic isotopic effect (KIE) was tested for both the HER and ECH on $\text{Mo}_2\text{C}@/\text{MoS}_2$, in terms of the ratio of current densities within H_2O and D_2O at -0.45 V vs. RHE (Fig. S21, ESI[†]). $\text{Mo}_2\text{C}@/\text{MoS}_2$ showed a value of 1.92 for the HER, higher than that for ECH (1.52) (Fig. 3g). It's suggested that the H^* is not the only determinant in the ECH. Meanwhile, the productivity of 4-VA on $\text{Mo}_2\text{C}@/\text{MoS}_2$ presented a positively logarithmical correlation with the initial 4-NS concentration (Fig. S22, ESI[†]), and the CVs of 4-NS showed a good linear correlation of anodic peak currents with scan rates (Fig. S23, ESI[†]), which together confirmed the nonnegligible contribution of 4-NS*.^{16,43} The strengthened 4-NS* adsorption on $\text{Mo}_2\text{C}@/\text{MoS}_2$ was evidenced by the more significant increase in open-circuit potential (73.1 mV) after injecting 4-NS into the blank electrolyte (Fig. S24, ESI[†]), as compared with those observed on Mo_2C (0.3 mV) and MoS_2 (26.5 mV). This experimental result consistent with our theoretical prediction (Fig. 1b) indicated the effective chemisorption and activation of the nitro group. According to the typical L–H mechanism, the conversion of 4-NS to 4-VA requires the co-participation of both 4-NS* and H^* , which thereby highly depends on the competitive adsorption of these two substrates. A strong 4-NS* adsorption will inevitably weaken one of the H^* and *vice versa*. As verified by the above experimental and theoretical results, the $\text{Mo}_2\text{C}-\text{MoS}_2$ interface is conducive to excellent catalytic performance because of its capability of balancing the competitive adsorption of H^* and 4-NS*.

We collected *in situ* Raman spectra on Mo_2C , $\text{Mo}_2\text{C}@/\text{MoS}_2$ and MoS_2 to understand their varied ECH performance (Fig. 4a–c). The initial spectra at 0 min exhibited two major signals at

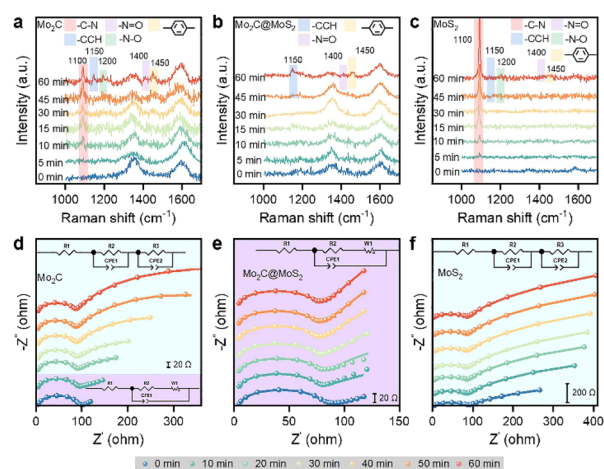
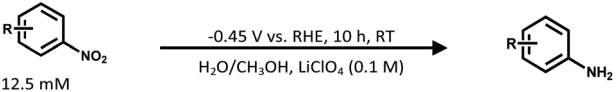


Fig. 4 (a–c) *In situ* Raman spectra and (d–f) Nyquist plots collected on (a and d) Mo_2C , (b and e) $\text{Mo}_2\text{C}@/\text{MoS}_2$, and (c and f) MoS_2 at -0.45 V vs. RHE.



Table 1 ECH of various functionalized nitroarenes over Mo₂C@MoS₂


R=Cl	FE 90% yield 88% (<i>m</i>)	FE 87% yield 72% (<i>p</i>)
R=Br	FE 84% yield 80% (<i>m</i>)	FE 86% yield 82% (<i>p</i>)
R=I	FE 99% yield 96% (<i>m</i>)	FE 99% yield 84% (<i>p</i>)
R=OCH ₃	FE 99% yield 92% (<i>m</i>)	FE 99% yield 88% (<i>p</i>)

about 1350 and 1600 cm⁻¹ attributing to the carbon matrix of Mo₂C and Mo₂C@MoS₂ (Fig. S25, ESI†). The ECH of 4-NS occurred as reaction time went on, and accordingly new bands appearing at 1100, 1200, 1400, 1450, and 1150 cm⁻¹ could be attributed to the stretching vibrations of C–N, N–O, N=O and benzene ring and the in-plane bending one of CCH, respectively (Table S3, ESI†).^{44,45} In detail, the band of C–N (1100 cm⁻¹) was detected after 5–10 min on Mo₂C and MoS₂, and its progressive enhancement on MoS₂ suggested the accumulation of 4-NS due to the strong chemisorption of 4-NS* but insufficient *H for the ECH. Owing to the relatively weaker binding with 4-NS* on Mo₂C, the C–N band increased slowly. Besides, the others assigned to CCH, N–O, N=O and benzene ring were due to the presence of intermediates, such as phenylhydroxylamine and nitroso benzene. By contrast, there were nearly no signals of 4-NS and intermediates detected on Mo₂C@MoS₂ before 60 min, confirming the rapid surface elementary steps of ECH involving the co-presented H* and 4-NS* on Mo₂C–MoS₂ interfaces.

Quasi *in situ* EIS, an efficient technique for identifying reaction interfaces, was performed at intervals during the ECH (Fig. 4d, e and S26, ESI†). The series resistance (*R*_s) was consistent over Mo₂C, Mo₂C@MoS₂ and MoS₂ (Table S4, ESI†), but the configurations at low frequencies were quite different, which were well-fitted with the varied equivalent circuit diagram. It's shown that the kinetic behavior of Mo₂C has changed from infinite diffusion to multiple interface diffusion after 20 min and MoS₂ kept the feature of multiple interface diffusion. In sharp comparison, Mo₂C@MoS₂ showed kinetic behavior approximating infinite diffusion, consistent with the result of *in situ* Raman spectroscopy. In other words, the consistent interfacial charge transfer on Mo₂C@MoS₂ is ascribed to the quickly refreshed active surface; however, those of Mo₂C and MoS₂ suffer from an extra interfacial impedance owing to reactant/intermediate accumulation on their surfaces.

We further examined the efficiency of Mo₂C@MoS₂ in wide substrate scope (Table 1) and analyzed the products by ¹H NMR (Fig. S27–S46, ESI†). For *meta* (*m*) and *para* (*p*)-halogenated nitrobenzenes (X = I, Br, Cl), Mo₂C@MoS₂ exhibited excellent performance with high FE (84–99%) and considerable yield (72–96%) of target halogenated anilines, in which the by-products of hydro-dehalogenation and H₂ were rarely detected. This demonstrated the extraordinary tolerance for halogen functional groups. Moreover, it achieved the excellent efficacy of ECH for nitroarenes with a methoxy group, keeping the high FE

(~99%) and yield (88–92%) of target anilines. These results verified the promise of Mo₂C@MoS₂ for the ECH of nitroarenes.

Conclusions

In summary, Mo₂C@MoS₂ heteronanostructures with dual sites were proposed to enable the efficient ECH of nitroarenes on synergized interfaces. As predicated using DFT calculations, the Mo₂C–MoS₂ interface can strengthen the binding of H* on Mo₂C and 4-NS* on nearby MoS₂, conducive for the successive hydrogenation toward the corresponding anilines. Mo₂C@MoS₂ achieved the high FE (>85%), yield (>78%) and selectivity (>99%) of 4-NS to value-added 4-VA, superior to Mo₂C and MoS₂. Accordingly, *in situ* Raman spectroscopy and quasi *in situ* EIS confirmed the facilitated chemisorption and further hydrogenation of 4-NS on Mo₂C–MoS₂ interfaces owing to the synergistically strengthened binding. Moreover, Mo₂C@MoS₂ delivered high efficiency for the ECH of nitroarenes to produce functional anilines in wide substrate scope. This work will provide new opportunities to develop high-performance electrocatalysts *via* the rational engineering of nanostructures and interfaces. Nevertheless, there still existed some challenges for ECH in comparison with thermo-catalysis, such as relatively lower space-time yield and immature reactor design. Drawing lessons from the mature experience of thermal-catalysis will expedite further progress in ECH.

Data availability

Data supporting the findings of this study are available within the article ESI.†

Author contributions

Wanling Zhang: synthesis, investigations, formal analysis, writing of the original draft, data curation. Wenbiao Zhang: writing-review and editing, DFT calculations, supervision. Kun Yu: experimental analysis, image polish. Jingwen Tan: proof-reading of the original draft. Yi Tang: conceptualization, supervision, funding acquisition. Qingsheng Gao: conceptualization, supervision, writing-review and editing, funding acquisition.

Conflicts of interest

There are no conflicts to declare.

Acknowledgements

This work was supported by the National Key R&D Program of China (2018YFA0209402), National Natural Science Foundation of China (grant No. 22175077), Innovation Team Project in Guangdong Colleges and Universities (2021KCXTD009), Guangzhou Science and Technology Project (202201020071), and Fundamental Research Funds for the Central Universities (No. 21623103).



Notes and references

- 1 P. De Luna, C. Hahn, D. Higgins, S. A. Jaffer, T. F. Jaramillo and E. H. Sargent, *Science*, 2019, **364**, eaav3506.
- 2 G. Papanikolaou, G. Centi, S. Perathoner and P. Lanzafame, *ACS Catal.*, 2022, **12**, 2861–2876.
- 3 C. Tang, Y. Zheng, M. Jaroniec and S.-Z. Qiao, *Angew. Chem., Int. Ed.*, 2021, **60**, 19572–19590.
- 4 C. Liu, Y. Wu, B. Zhao and B. Zhang, *Acc. Chem. Res.*, 2023, **56**, 1872–1883.
- 5 C. Han, J. Zenner, J. Johnny, N. Kaeffer, A. Bordet and W. Leitner, *Nat. Catal.*, 2022, **5**, 1110–1119.
- 6 S. A. Akhade, N. Singh, O. Y. Gutiérrez, et al., *Chem. Rev.*, 2020, **120**, 11370–11419.
- 7 L. Zhang, T. U. Rao, J. Wang, D. Ren, S. Sirisommoonchai, C. Choi, H. Machida, Z. Huo and K. Norinaga, *Fuel Process. Technol.*, 2022, **226**, 107097.
- 8 P. Zhou, L. Li, V. S. S. Mosali, Y. Chen, P. Luan, Q. Gu, D. R. Turner, L. Huang and J. Zhang, *Angew. Chem., Int. Ed.*, 2022, **61**, e202117809.
- 9 J. T. Kleinhaus, J. Wolf, K. Pellumbi, L. Wickert, S. C. Viswanathan, K. Junge Puring, D. Siegmund and U.-P. Apfel, *Chem. Soc. Rev.*, 2023, **52**, 7305–7332.
- 10 J. Song, Z.-F. Huang, L. Pan, K. Li, X. Zhang, L. Wang and J.-J. Zou, *Appl. Catal., B*, 2018, **227**, 386–408.
- 11 H. Jin, P. Li, P. Cui, J. Shi, W. Zhou, X. Yu, W. Song and C. Cao, *Nat. Commun.*, 2022, **13**, 723.
- 12 Y. Ren, Y. Tang, L. Zhang, et al., *Nat. Commun.*, 2019, **10**, 4500.
- 13 P. Deng, J. Duan, F. Liu, et al., *Angew. Chem., Int. Ed.*, 2023, **62**, e202307853.
- 14 G. Liu, C. Chen and J. Chen, *J. Phys. Chem. C*, 2023, **127**, 4375–4386.
- 15 R. Xia, D. Tian, S. Kattel, B. Hasa, H. Shin, X. Ma, J. G. Chen and F. Jiao, *Nat. Commun.*, 2021, **12**, 1949.
- 16 J. Tan, J. Shao, Y. Shi, W. Zhang and Q. Gao, *ACS Sustain. Chem. Eng.*, 2022, **10**, 13525–13533.
- 17 J. A. Lopez-Ruiz, E. Andrews, S. A. Akhade, et al., *ACS Catal.*, 2019, **9**, 9964–9972.
- 18 J. Tan, W. Zhang, Y. Shu, H. Lu, Y. Tang and Q. Gao, *Sci. Bull.*, 2021, **66**, 1003–1012.
- 19 J. Anibal and B. Xu, *ACS Catal.*, 2020, **10**, 11643–11653.
- 20 C. Liu, R. Li, W. Zhou, et al., *ACS Catal.*, 2021, **11**, 8958–8967.
- 21 U. Sanyal, S. F. Yuk, K. Koh, et al., *Angew. Chem., Int. Ed.*, 2021, **60**, 290–296.
- 22 H. Wu, J. Song, C. Xie, Y. Hu, P. Zhang, G. Yang and B. Han, *Chem. Sci.*, 2019, **10**, 1754–1759.
- 23 S. Huang, B. Gong, Y. Jin, P. H.-L. Sit and J. C.-H. Lam, *ACS Catal.*, 2022, **12**, 11340–11354.
- 24 S. Wang, D. Zhang, B. Li, C. Zhang, Z. Du, H. Yin, X. Bi and S. Yang, *Adv. Energy Mater.*, 2018, **8**, 1801345.
- 25 J. Liu, Y. Zheng, D. Zhu, A. Vasileff, T. Ling and S.-Z. Qiao, *Nanoscale*, 2017, **9**, 16616–16621.
- 26 T. Yang, T. T. Song, J. Zhou, S. Wang, D. Chi, L. Shen, M. Yang and Y. P. Feng, *Nano Energy*, 2020, **68**, 104304.
- 27 Z. Shi, X. Zhang, X. Lin, et al., *Nature*, 2023, **621**, 300–305.
- 28 K. Pellumbi, L. Wickert, J. T. Kleinhaus, et al., *Chem. Sci.*, 2022, **13**, 12461–12468.
- 29 Q. Gao, W. Zhang, Z. Shi, L. Yang and Y. Tang, *Adv. Mater.*, 2019, **31**, 1802880.
- 30 L. Lin, W. Zhou, R. Gao, et al., *Nature*, 2017, **544**, 80–83.
- 31 X. Fan, C. Liu, M. Wu, et al., *Appl. Catal., B*, 2022, **318**, 121867.
- 32 H. Lin, Z. Shi, S. He, X. Yu, S. Wang, Q. Gao and Y. Tang, *Chem. Sci.*, 2016, **7**, 3399–3405.
- 33 B. Q. Lv, H. M. Weng, B. B. Fu, et al., *Phys. Rev. X*, 2015, **5**, 031013.
- 34 Y. Sun, A. J. Darling, Y. Li, K. Fujisawa, C. F. Holder, H. Liu, M. J. Janik, M. Terrones and R. E. Schaak, *Chem. Sci.*, 2019, **10**, 10310–10317.
- 35 Y. Zhao, C. Liu, C. Wang, X. Chong and B. Zhang, *CCS Chem.*, 2021, **3**, 507–515.
- 36 H. Li, Y. Gao, Y. Wu, C. Liu, C. Cheng, F. Chen, Y. Shi and B. Zhang, *J. Am. Chem. Soc.*, 2022, **144**, 19456–19465.
- 37 Y. Shu, L. Zhang, H. Cai, Y. Yang, J. Zeng, D. Ma and Q. Gao, *Sens. Actuators, B*, 2020, **311**, 127863.
- 38 J. M. Mayer, *J. Am. Chem. Soc.*, 2023, **145**, 7050–7064.
- 39 W. Zhang, W. Zhang, J. Tan, D. Pan, Y. Tang and Q. Gao, *J. Mater. Chem. A*, 2023, **11**, 7505–7512.
- 40 X. Chong, C. Liu, Y. Huang, C. Huang and B. Zhang, *Natl. Sci. Rev.*, 2020, **7**, 285–295.
- 41 S. Wu, X. Huang, H. Zhang, Z. Wei and M. Wang, *ACS Catal.*, 2021, **12**, 58–65.
- 42 M. Li, C. Liu, Y. Huang, S. Han and B. Zhang, *Chin. J. Catal.*, 2021, **42**, 1983–1991.
- 43 Y. Zheng, Z. Wang, P. Chen, W. Zhang and Q. Gao, *ChemSusChem*, 2023, **16**, e202300180.
- 44 J. Ma, Z. Wang, T. Majima and G. Zhao, *ACS Catal.*, 2022, **12**, 14062–14071.
- 45 X.-M. Zhu, S.-Q. Zhang, X. Zheng and D. L. Phillips, *J. Phys. Chem. A*, 2005, **109**, 3086–3093.

